

Cosmic-ray pressure driven magnetic field amplification: dimensional, radiative and field orientation effects.

T. P. Downes^{1,2,3} and L. O’C. Drury²

<mailto:turlough.downes@dcu.ie>

<mailto:ld@cp.dias.ie>

¹School of Mathematical Sciences, Dublin City University,
Glasnevin, Dublin 9, Ireland

²School of Cosmic Physics, Dublin Institute for Advanced Studies,
31 Fitzwilliam Place, Dublin 2, Ireland

³National Centre for Plasma Science and Technology,
Dublin City University, Glasnevin, Dublin 9, Ireland

September 15, 2018

Abstract

Observations of non-thermal emission from several supernova remnants suggest that magnetic fields close to the blastwave are much stronger than would be naively expected from simple shock compression of the field permeating the interstellar medium (ISM). We investigate in some detail a simple model based on turbulence generation by cosmic-ray pressure gradients. Previously this model was investigated using 2D MHD simulations.

Motivated by the well-known qualitative differences between 2D and 3D turbulence, we further our investigations of this model using both 2D and 3D simulations to study the influence of the dimensionality of the simulations on the field amplification achieved. Further, since the model implies the formation of shocks which can, in principle, be efficiently cooled by collisional cooling we include such cooling in our simulations to ascertain whether it could increase the field amplification achieved. Finally, we examine the influence of different orientations of the magnetic field with respect to the normal of the blastwave.

We find that dimensionality has a slight influence on the overall amplification achieved, but a significant impact on the morphology of the amplified field. Collisional cooling has surprisingly little impact, primarily due to the short time which any element of the ISM resides in the precursor region for supernova blastwaves. Even allowing for a wide range of orientations of the magnetic field, we find that the magnetic field can be expected to be amplified by, on average, *at least* an order of magnitude in the precursors of supernova blastwaves.

1 Introduction

The properties of the non-thermal emission observed in various supernova remnants suggest that the strength of magnetic fields in the vicinity of the blastwave is significantly more than would be expected from either the typical field strength in the interstellar medium (ISM), or the strength of that which would be achieved by simple shock compression (Vink & Laming, 2003; Berezhko et al., 2003; Bamba et al., 2004, 2005; Völk et al., 2005; Ballet, 2006; Parizot et al., 2006; Vink, 2012; Uchiyama et al., 2007; Yamazaki et al., 2004). The presence of such amplified fields could fill in a missing piece in the theory of cosmic ray acceleration by SNR shocks and allow acceleration to the energies needed to explain the cosmic-ray ‘knee’ particles; if the magnetic field strength is only a few μG as expected in the interstellar medium it is very hard to get the acceleration to reach these energies as pointed out by Lagage & Cesarsky (1983).

We must then try to understand what physical process might give rise to such field amplification. An attractive idea is that in which magnetic fields might be amplified to the required degree by cosmic-ray driven processes themselves, specifically those processes occurring in strong shocks bounding young supernova remnants (SNRs). Indeed, in the work of Bell (2004) it was pointed out that the existence of a strong current-driven instability under conditions thought to be appropriate to young remnants can amplify magnetic fields. The Bell instability appears to be capable of acting in the precursor regions of SNR shocks but unfortunately only acts on short length-scales and, in the absence of some inverse cascade of energy, thus cannot create the necessary relatively large length-scale field amplification required to explain the observations. Another candidate is the instability identified in Drury & Falle (1986) and further studied in Begelman & Zweibel (1994) (*cf* also Webb et al. (1999) and Ryu et al. (1993)). This has the advantage of operating on scales large compared to the gyro-radius of the driving particles and in relying only on rather simple and robust physics.

In Drury & Downes (2012, hereafter Paper I), we presented a simple model in which the cosmic ray pressure gradient drives turbulence in the precursor of the blastwave through inducing differential acceleration on the inhomogeneous ISM through which the blastwave and precursor are moving, similar to an idea proposed by Beresnyak et al. (2009). This differential acceleration occurs by virtue of the fact that the ISM contains density variations resulting from pre-existing turbulence. The cosmic ray pressure gradient exerts a body force on the ISM which is independent of density and the resulting differential acceleration induces strong shear in the flow which, through fluid instabilities, creates turbulence. This turbulence stretches and twists the magnetic field permeating the ISM creating enhanced field strengths throughout the precursor and, indeed, in the medium behind the supernova blastwave.

A particularly attractive property of this model is that it acts on large length scales - lengths comparable to the diffusion lengths of the highest energy non-thermal particles accelerated at the blastwave. Thus, the amplification of the magnetic fields resulting from this process will occur on roughly these length scales also and, therefore, have the potential to explain the observations of narrow filaments of non-thermal emission in the X-ray (Vink, 2012).

In Paper I we presented 2D simulations in which we examined the action of the proposed process to ascertain whether or not it could plausibly produce the required magnetic

field strengths. It was found that, indeed, significant field amplification can occur, up to at least a factor of 20 for the conditions studied. In this work we extend the exploration of this model in several directions as follows:

- Turbulence in three dimensions (3D) is fundamentally different to two dimensional (2D) turbulence in that the energy cascade in 3D is from large length scales to small ones, while in 2D the reverse is the case. It is important to ascertain whether or not this influences the likely relevance of the process proposed in our toy model.
- While radiative cooling through line emission is unimportant in the blastwaves of young SNRs, the differential acceleration produced under the proposed process will yield shock strengths which produce conditions under which such radiative cooling may well be significant. Such cooling will change the nature of the density inhomogeneities, and therefore the differential acceleration, in the precursor and so might also effect the field amplification achieved.
- The angle of the mean magnetic field to the normal of the blastwave is an important factor in amplification. One may expect that a perpendicular shock will result in much stronger field amplification than a parallel shock. Note that we do not include here the effects of the angle of the field on the diffusion coefficient for the cosmic ray particles. This is undoubtedly an important effect, but its influence is hard to gauge given the highly tangled nature of the magnetic field in the precursor region.

Brüggen (2013) have also investigated the model presented in Paper I, mainly focusing on how the model might work for cosmic ray precursors of intracluster shocks. This latter work employed both 2D and 3D simulations to investigate the amplification factors achieved for low Mach number ($M \approx 2 - 3$) and high Mach number ($M = 100$) shocks. The results confirmed our original results. Interestingly, this work detected no major difference in the field amplification achieved in 2D and 3D simulations. We return to this point in Sect. 4.1.

The layout of this paper is as follows: in section 2 we briefly describe the toy model introduced in Paper I; in section 3 we describe our approach to studying the model; while in section 4 we address each of the issues raised above in turn. Finally we give our conclusions in section 5.

2 Recapitulation of the toy model

The instability which is the basis for the proposed mechanism of amplifying the magnetic field in the precursor of SNR shocks comes about because the cosmic ray pressure gradient in this precursor exerts a ponderomotive force which is independent of density on the ISM passing through the precursor. Any pre-existing density fluctuations in the ISM will thus result in differential acceleration, inducing shear which then creates turbulence through various instabilities such as the Kelvin-Helmholtz instability. This turbulence then amplifies the pre-existing magnetic field in the usual way through stretching and folding the field lines. Thus the whole system acts as a dynamo, converting the energy of the cosmic rays into magnetic energy in the precursor region.

In order to attempt to model this process we make the rather drastic assumption that the cosmic ray propagation is completely decoupled from the matter dynamics. While this assumption clearly omits a lot of important physics, it will nonetheless allow us to model the system to give some insight into how such a process could influence the strength of the magnetic field. In fact, this assumption is likely to result in an *underestimate* of the efficacy of the process in amplifying the magnetic field as cosmic ray particles are likely to diffuse more effectively along channels already evacuated by increased cosmic ray pressure, resulting in an enhanced instability and therefore stronger field amplification.

We assume a linear cosmic ray pressure in the precursor and consider a system consisting of a rectangular computational box extending in the x -direction from 0 to L within which the cosmic ray pressure P_C rises linearly from zero at the inflow side to a value of order the ram pressure of the inflowing plasma at the outflow side. The shock position is thus taken to be at $x = L$ and

$$P_C(x) = \theta \rho_0 U_0^2 \frac{x}{L}, \quad (1)$$

where $0 < \theta < 1$ is a positive parameter less than unity.

As a result of this pressure gradient the flow is decelerated by a uniform body force $-\theta \rho_0 U_0^2 / L$. The flow is seeded with small-scale density fluctuations with a log-normal distribution, which is what would be expected from isothermal turbulence in the ISM.

Presuming the incoming flow contains density irregularities of magnitude $\delta\rho$ on a length scale λ the bulk force, operating on a time scale of order the advection time through the precursor, will generate velocity fluctuations of magnitude

$$\delta u \approx \frac{\delta\rho}{\rho_0} \frac{1}{\rho_0} \frac{\theta \rho_0 U_0^2}{L} \frac{L}{U_0} \approx \frac{\delta\rho}{\rho_0} \theta U_0 \quad (2)$$

on the same length scale λ . If this is to drive turbulence we require the eddy turn-over time to be short compared to the outer-scale and thus

$$\frac{\lambda}{\delta u} \ll \frac{L}{U_0} \Rightarrow \lambda \ll \theta \frac{\delta\rho}{\rho_0} L \quad (3)$$

Density fluctuations satisfying this not very restrictive condition should be capable of inducing turbulence and thus magnetic field amplification. The total amount of kinetic energy available in the turbulence can be roughly estimated as

$$e_F = \frac{1}{2} \rho_0 (\delta u)^2 \approx \frac{1}{2} (\delta\rho)^2 \theta^2 U_0^2 \quad (4)$$

and thus the maximum amplified field should be below full equipartition by a factor of order $\theta^2 (\delta\rho/\rho_0)^2$. If nonlinear effects drive the density fluctuations to saturation at $\delta\rho \approx \rho$ (as is probable) then this process could be very efficient at converting flow energy into magnetic energy if $\theta \approx 1$.

3 Numerical method

As in [Paper I](#), we use the *HYDRA* code ([O'Sullivan & Downes, 2006, 2007](#)), configured for simulating ideal MHD flows rather than multifluid MHD systems, to study this model.

The equations solved are

$$\frac{\partial \rho}{\partial t} + \nabla \cdot (\rho \mathbf{u}) = 0 \quad (5)$$

$$\frac{\partial \rho \mathbf{u}}{\partial t} + \nabla \cdot (\rho \mathbf{u} \mathbf{u} + P \mathbf{I}) = \mathbf{J} \times \mathbf{B} + \mathbf{F}_{\text{cr}}, \quad (6)$$

$$\begin{aligned} \frac{\partial e}{\partial t} + \nabla \cdot [(e + P) \mathbf{u}] &= \mathbf{J} \cdot (\mathbf{u} \times \mathbf{B}) + \mathbf{F}_{\text{cr}} \cdot \mathbf{u} \\ &\quad - n^2 \Lambda(T) \end{aligned} \quad (7)$$

$$\frac{\partial \mathbf{B}}{\partial t} + \nabla \cdot (\mathbf{u} \mathbf{B} - \mathbf{B} \mathbf{u}) = 0, \quad (8)$$

$$\nabla \cdot \mathbf{B} = 0 \quad (9)$$

where ρ is the mass density, n is the number density, \mathbf{u} is the fluid velocity, P is the thermal pressure, \mathbf{B} is the magnetic field, \mathbf{F}_{cr} is the force due to the cosmic ray pressure gradient and \mathbf{I} is the identity matrix. \mathbf{F}_{cr} is given by

$$\begin{aligned} \mathbf{F}_{\text{cr}} &= -\nabla P_{\text{C}} \\ &= -\frac{\theta \rho_0 U_0^2}{L} \hat{\mathbf{B}} \end{aligned} \quad (10)$$

(see equation 1).

The final term on the right hand side of equation 7 is that for radiative losses due to collisional cooling. Implicit in using this functional form for the cooling is that the ISM is dominated by atomic hydrogen which is fully ionised. There is some inaccuracy in this approximation. However, we deal with this as follows. First, a fit was performed to the data in [Sutherland & Dopita \(1993\)](#) for non-equilibrium cooling for a gas with solar abundances. This fit was for a 6th order polynomial. This high order was found to be necessary to capture sufficiently accurately (see below) one of the most important properties of the function: its slope as a function of temperature. The resulting cooling function was tested using the overstable radiative shock test (e.g. [Gaetz et al., 1988](#)) and modified slightly in order to bring the test results into agreement with the published data for this test. Thus Λ is calculated as follows. Set $\alpha = \log_{10} T$ and

$$\begin{aligned} g(T) &= -0.651597\alpha^6 + 20.2803\alpha^5 - 261.438\alpha^4 + 1786.93\alpha^3 \\ &\quad - 6831.53\alpha^2 + 13856.8\alpha - 11678.9. \end{aligned} \quad (11)$$

Then

$$\Lambda(T) = 10^{g(T)}. \quad (12)$$

These equations are advanced in time using a standard van Leer-type second order, finite volume, shock capturing scheme. The magnetic field divergence is controlled using the method of [Dedner et al. \(2002\)](#). The unusual form of the MHD equations used here is due to *HYDRA* being a multifluid code, making this form of the equations more convenient. This code has been extensively validated for both multifluid and ideal MHD set-ups ([O'Sullivan & Downes, 2007, 2006](#)) and see also Appendix A.

For the simulations presented in this work we take θ (defined in equation 1) to be 0.6 which is observationally reasonable (e.g. [Vink, 2012](#), and references therein). For the large Mach numbers associated with supernova blastwaves this will give us a very significant acceleration of the pre-shock flow.

3.1 Set-up of the problem

We proceed as in [Paper I](#), formulating the problem in the rest frame of the blastwave which is assumed to be planar. For the purposes of this work we present our initial conditions in physical, rather than dimensionless units. The principle reason for this is that we will be studying the effects of radiative (line) cooling on the flow and hence it makes more sense to leave aside dimensionless parameters. The speed of the blastwave is taken to be $2.9 \times 10^8 \text{ cm s}^{-1}$ and the mean temperature of the ISM is taken to be 10^4 K , assuming solar abundances. This yields a Mach number for the blastwave of 290. The position of the blastwave is at $x = L$ where we take $L = 5 \times 10^{17} \text{ cm}$ for this work. The size of the computational domain is $L \times \frac{L}{8} \times \frac{L}{8}$ (for 3D simulations) and $L \times \frac{L}{8}$ for 2D simulations. Thus the blastwave is positioned at the boundary of our domain, and is not actually part of the calculations at all, as is appropriate since we are interested only in the precursor region. The initial magnetic field in the ISM is taken to be uniform and of strength $3 \mu\text{G}$ while the mean density of the ISM is set at $\rho_0 = 2.3 \times 10^{-22} \text{ g cm}^{-3}$, or 100 cm^{-3} unless otherwise stated. The density distribution in the ISM is prescribed as in [Paper I](#), having an RMS variation of 0.2 and a log-normal distribution. The pressure is taken to be uniform, yielding the mean temperature given above.

Using the resolution study presented in [Paper I](#) we know that, while this system cannot be fully resolved unless simulations resolving the dissipation scale (either viscous or resistive or both) are performed, a resolution of 2000×250 is adequate for this set-up. Hence all 2D simulations presented here have a resolution of 2000×250 unless otherwise stated, while 3D simulations have a resolution of $2000 \times 250 \times 250$. The only case one might be concerned about is that where radiative cooling is present. Cooling introduces new length and time-scales and these must be well resolved in order to be reasonably confident of the results of the simulations. Therefore we performed extensive validation simulations in 2D with resolutions up to 4000×500 for the radiatively cooled simulations and found that, indeed, simulations including this effect can be adequately resolved at 2000×250 . Note, however, that if a higher ISM density is used this conclusion will no longer be valid since the cooling length goes as the inverse of the square of the density.

In order to study the influence of radiative cooling, the dimensionality of the system and the influence of the angle of the field to the shock normal we performed a suite of simulations as detailed in [Table 1](#). Note that the field angle is measured with respect to the normal of the blastwave.

3.2 Boundary conditions

The boundary conditions are set as follows:

- The left-hand boundary, where pre-shock ISM flows into the computational domain, is a forced boundary with velocity $2.9 \times 10^8 \text{ cm s}^{-1}$. The density here is time dependent and defined such that the random density distribution flowing onto the grid matches that on the grid at $t = 0$ and has a (spatial) periodicity of L .
- The right-hand boundary, where pre-shock ISM flows off the grid, is set to gradient zero boundary conditions. This is appropriate as the ISM is still flowing supersonically at this point and so any waves emitted from this boundary as a result of the imposition of the gradient zero boundary conditions will be carried off the grid.

Table 1: Summary of the simulations presented in this work

Simulation	Field angle	Dimension	Grid size	Notes
adb-2d-std-lr	$\frac{\pi}{2}$	2D	1000×125	Adiabatic
adb-2d-std	$\frac{\pi}{2}$	2D	2000×250	Adiabatic
adb-2d-std-hr	$\frac{\pi}{2}$	2D	4000×500	Adiabatic
adb-3d-std	$\frac{\pi}{2}$	3D	$2000 \times 250 \times 250$	Adiabatic
cool-2d-std	$\frac{\pi}{2}$	2D	2000×250	Radiatively cooled
cool-2d-hden	$\frac{\pi}{2}$	2D	2000×250	Radiatively cooled, $\rho_0 = 10^3 \text{ cm}^{-3}$
cool-3d-std	$\frac{\pi}{2}$	3D	$2000 \times 250 \times 250$	Radiatively cooled
adb-2d-b00	0	2D	2000×250	Adiabatic
adb-2d-b30	$\frac{\pi}{6}$	2D	2000×250	Adiabatic
adb-2d-b60	$\frac{2\pi}{6}$	2D	2000×250	Adiabatic

- All other boundaries are set to periodic.

With these boundary conditions we are effectively simulating an infinite domain in the y (and z) directions, with the restriction that wavelengths longer than $L/8$ can not be represented.

4 Results

We now discuss the results of our simulations. Figures 1 and 2 contain plots of the distribution of magnetic field strength and vorticity at $t = 10^{15}$ s for simulations adb-2d-std, adb-3d-std, cool-2d-std and cool-2d-hden. It is clear that the nature of the turbulence generated in each of the 2D simulations is rather similar, resulting in large-scale structures while the turbulence in adb-3d-std involves somewhat smaller scale structures. Even in the latter case, the scales on which the field amplification occurs are still long in comparison to those of, for example, the Bell instability. The qualitative differences between 2D and 3D turbulence are discussed in more detail in Sect. 4.1.

Following the discussion in Sect. 1, we split our results into discussions of the influence of dimensionality (Sect. 4.1), the orientation of the magnetic field (Sect. 4.2) and the influence of radiative cooling (Sect. 4.3).

4.1 Influence of dimensionality

We begin by examining the influence of dimensionality on the field amplification predicted by our toy model. As mentioned above, this is an essential element in the study because of the qualitative differences between 2D and 3D turbulence.

As can be seen from Fig. 3 there is a difference in the amplification of the magnetic field achieved between the 2D and 3D simulations. Significantly, the 2D system achieves a slightly higher (approximately 17%) maximum amplification. The extra variations seen in the plot of amplification for adb-2d-std are due to the averaging being over a smaller number of grid zones than in adb-3d-std, since averaging in the latter is over a 2D area, while averaging in the former is over a 1D line.

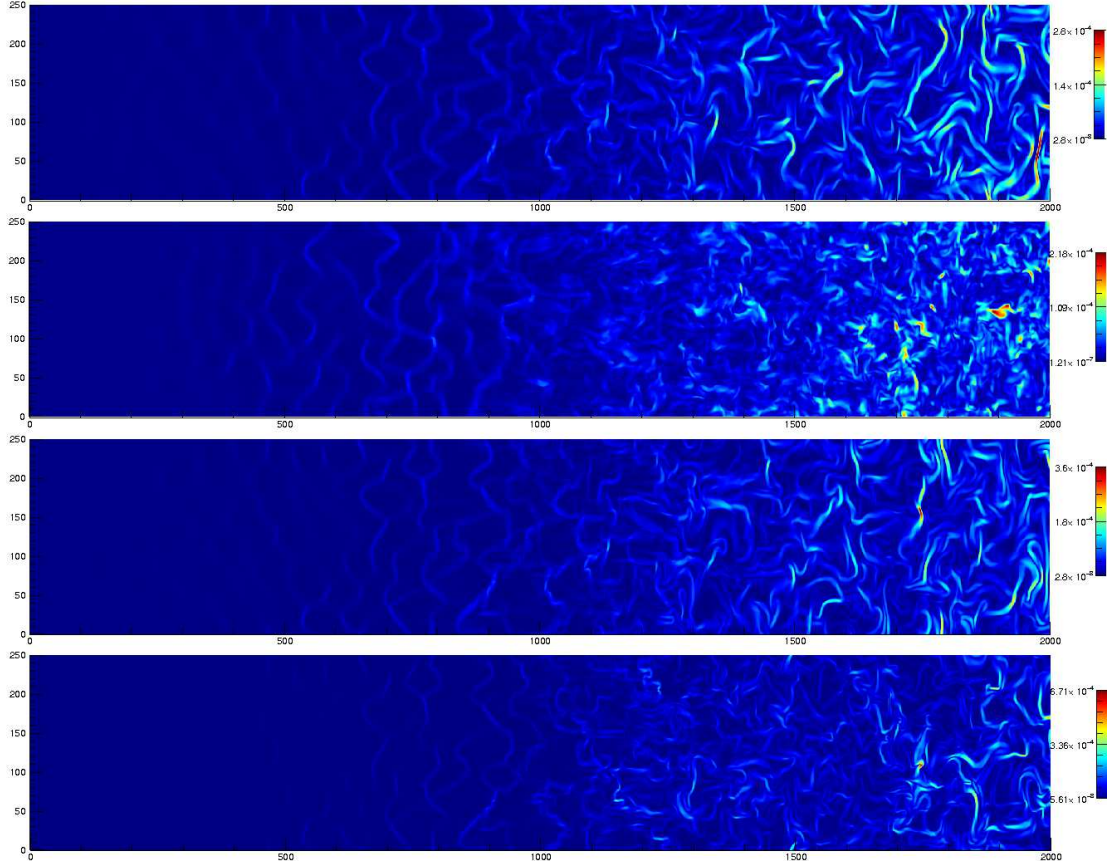


Figure 1: Plots of the magnetic field strength for adb-2d-std, adb-3d-std, cool-2d-std, cool-2d-std-hden at $t = 10^{15}$ s. For adb-3d-std the image is of a slice of the simulation at $z = 0$. It is clear that the magnetic field becomes highly distorted and amplified by the turbulence as it propagates through the precursor region. The units of field strength are μG , and the units of distance are 2.5×10^{14} cm (i.e. grid zone size).

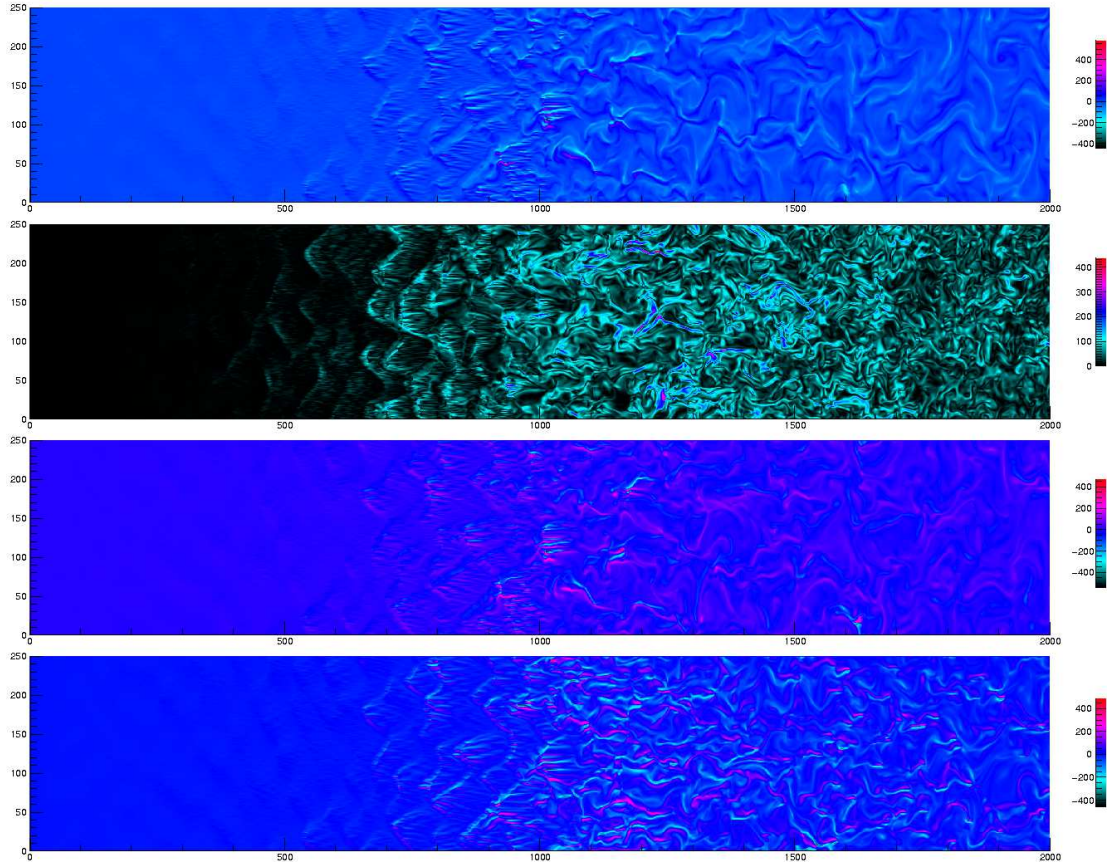


Figure 2: As Figure 1, but for vorticity (normalised by the flow time across the domain: L/U_0). For adb-3d-std the magnitude of the vorticity is plotted for the slice of the simulation at $z = 0$. The vorticity tends to peak towards the centre of the domain, then falls off as the ISM flows towards the right boundary.

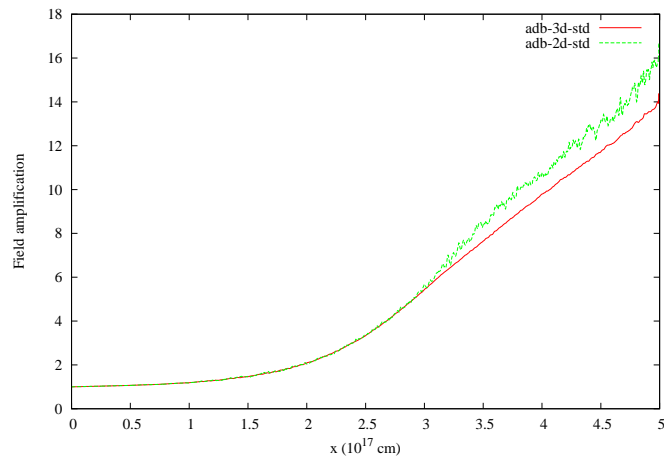


Figure 3: Plots of the magnetic field amplification, averaged over $0 \leq y \leq \frac{L}{8}$, for simulations adb-2d-std and adb-3d-std. Note that the 3D simulation achieves slightly lower amplification than the 2D one.

In order to understand the difference in the field amplification we can note that in a 3D (magneto)fluid system turbulent energy cascades from large scales to ever smaller scales until, finally, the viscous (or resistive) length scale is reached and the turbulent kinetic energy is then converted to heat. Hence the differential velocity, and therefore the turbulent kinetic energy, decreases with length scale. Thus one expects that, unless the magnetic field is very weak, at some length scale the kinetic energy density associated with turbulent motion will fall below that of the magnetic energy density. Below this length scale the fluid motions will not be able to efficiently stretch and twist the magnetic field, leading to a suppression of field amplification. The same system in 2D, on the other hand, suffers a turbulent energy cascade from small to larger length scales (see Figure 1). Thus as the turbulence develops energy concentrates at large length scales, corresponding to high turbulent kinetic energy densities. Hence, as the turbulence develops it is not suppressed as it is in 3D. It is worth noting that this idealised picture of turbulence should be considered only as an illustration: in fact the details of MHD turbulence are rather different to that of hydrodynamic turbulence, and the turbulence in the system under examination here is driven at *short* length scales. However, the description above suffices to give an intuitive understanding of the physical processes at work.

To illustrate the differences (in k -space) between the 2D and 3D systems, Figure 4 contains power spectra of the velocity in simulations adb-2d-std and adb-3d-std in the final eighth of the grid (i.e. the region defined by $4.375 \times 10^{17} \text{ cm} < x < 5 \times 10^{17} \text{ cm}$) where the turbulence will be well developed. It is clear that at low wavenumbers (large length scales) there is more power in the velocity variations in 2D than in 3D. On the other hand, at intermediate wavenumbers adb-3d-std has more power. As noted in Downes (2012), numerical diffusion begins to have a significant effect on velocity power spectra from the *HYDRA* code at wavelengths of less than about 10 – 15 zones, corresponding to wavenumbers in Figure 4 of greater than 15 – 25. Even so, it is clear that adb-3d-std exhibits more power at high k than adb-2d-std, just as expected from general discussions of the differences between 2D and 3D turbulence. To get some idea of the influence of resolution on our power spectra, in Figure 5 we present power spectra of the velocity in the region defined by $4.375 \times 10^{17} \text{ cm} < x < 5 \times 10^{17} \text{ cm}$ for adb-2d-std-lr, adb-2d-std and adb-2d-std-hr. It is apparent that, at least in the range $k \leq 15$ the results from adb-2d-std and adb-2d-std-hr are similar, as expected. Figures 6 and 7 illustrate the inverse cascade seen in 2D as opposed to 3D: the slope of the power spectrum in Region B ($4.375 \times 10^{17} \text{ cm} < x < 5 \times 10^{17} \text{ cm}$) is steeper around $k = 10$ than it is in Region A ($1.875 \times 10^{17} \text{ cm} \leq x \leq 2.5 \times 10^{17} \text{ cm}$) for adb-2d-std, while the reverse is true for simulation adb-3d-std. Hence, as the turbulence develops in the precursor region energy is transported across lengthscales in very much the way one would expect from a naive extension of incompressible hydrodynamic turbulence.

In summary, though, the dimensionality of the simulations, while clearly influencing the nature of the turbulence, only has a minor impact on the degree of magnetic field amplification achieved. This is largely in agreement with the conclusion of Brüggén (2013) who detected no difference in amplification factors between 2D and 3D. As described above, however, one would expect a qualitative difference in the morphology of the amplified field, and a small quantitative difference in the degree of amplification achieved, between 2D and 3D.

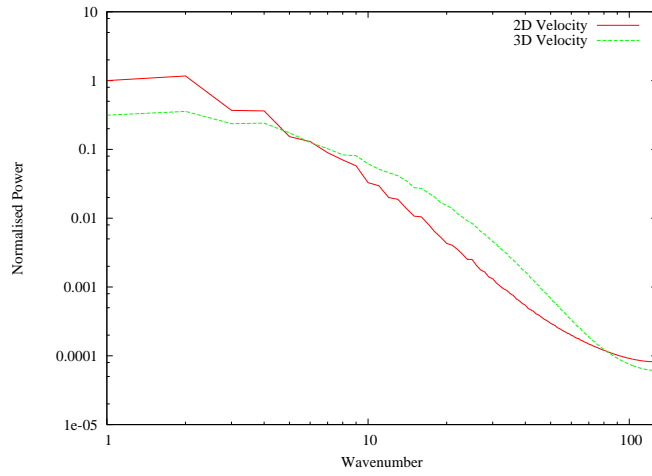


Figure 4: Plots of the power spectrum of the velocity for the region of the computational domain defined by $4.375 \times 10^{17} \text{ cm} < x < 5 \times 10^{17} \text{ cm}$ for simulations adb-2d-std and adb-3d-std.

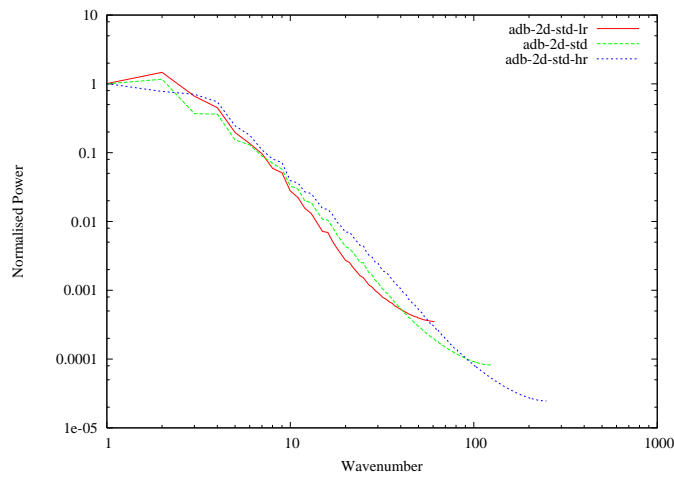


Figure 5: Plots of the power spectrum of the velocity for the region of the computational domain defined by $4.375 \times 10^{17} \text{ cm} < x < 5 \times 10^{17} \text{ cm}$ for simulations adb-2d-std-lr and adb-2d-std and adb-2d-std-hr.

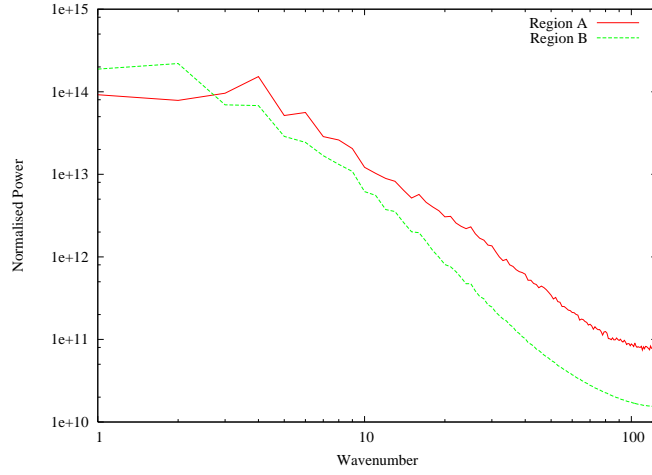


Figure 6: Plots of the power spectrum of the velocity for adb-2d-std in different regions of the simulations. Region A is defined by $1.875 \times 10^{17} \text{ cm} \leq x \leq 2.5 \times 10^{17} \text{ cm}$ and Region B is defined by $4.375 \times 10^{17} \text{ cm} < x < 5 \times 10^{17} \text{ cm}$. An inverse cascade is apparent, with the slope of the power spectrum in Region B being steeper than that in Region A.

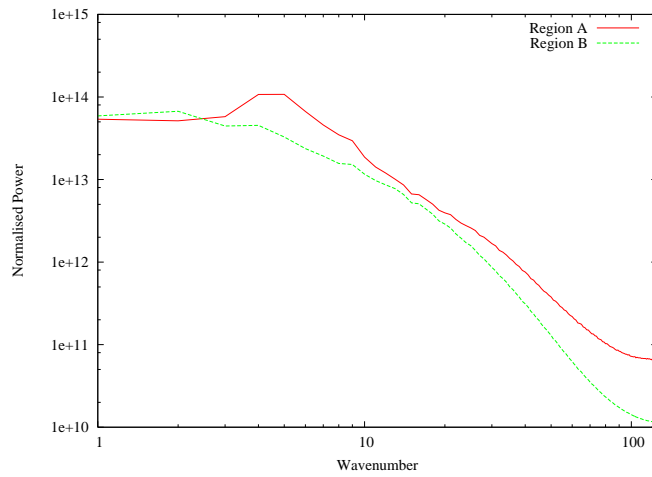


Figure 7: As Fig. 6 but for simulation adb-3d-std.

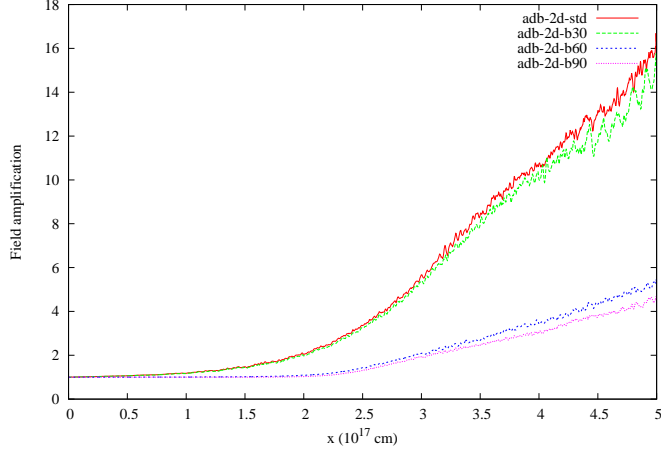


Figure 8: Plots of the magnetic field amplification, averaged over $0 \leq y \leq \frac{L}{8}$, for simulations with different initial angles of the magnetic field to the direction of flow.

4.2 Angle of magnetic field

We now turn our attention to the influence of the direction of the magnetic field amplification. In [Paper I](#), and for our standard simulations presented here, we start with a magnetic field which is oriented perpendicular to the shock normal - i.e. we model a perpendicular shock. Clearly this is the most favourable configuration for magnetic field amplification: the differential acceleration resulting from the interaction of the ISM with the cosmic ray pressure gradient immediately begins to shear the magnetic field lines, leading to amplification. If we consider the other extreme, where we model a parallel shock, the differential acceleration (at least initially) has no impact at all on the magnetic field strength.

Figure 8 shows plots of the magnetic field amplification as a function of distance for simulations adb-2d-b00, adb-2d-b30, adb-2d-b60 and adb-2d-std. It is very clear that the angle between the initial (i.e. mean) magnetic field and the direction of flow has a large impact on the field amplification achieved. The results here are not unexpected. To see this let us make the somewhat radical simplification that only the transverse component of the initial magnetic field contributes to the amplification. Then

$$\mathbf{B}_0 = B_0 \cos \alpha \hat{i} + B_0 \sin \alpha \hat{j} \quad (13)$$

and

$$\mathbf{B}_f = B_0 \cos \alpha \hat{i} + F B_0 \sin \alpha \hat{j} \quad (14)$$

where \mathbf{B}_f is the final magnetic field, α is the angle of the field to the normal of the shock and F can be measured from adb-2d-std (in which $\alpha = \frac{\pi}{2}$). We thus find that $F \approx 15$ and, defining $B_0 \equiv |\mathbf{B}_0|$ and $B_f \equiv |\mathbf{B}_f|$, so

$$\left. \frac{B_f}{B_0} \right|_{\alpha=60^\circ} \approx [0.75 + 0.25F^2]^{1/2} = 7.54 \quad (15)$$

$$\left. \frac{B_f}{B_0} \right|_{\alpha=30^\circ} \approx [0.25 + 0.75F^2]^{1/2} = 13 \quad (16)$$

which is indeed roughly what is seen in Fig. 8.

Thus our radical simplification does indeed appear to reflect something of the reality of the system: the transverse component of the magnetic field dominates the effective amplification achieved. Of course, there are clearly inaccuracies in this approximation: if there were none then simulation adb-2d-b00 would exhibit no field amplification whatsoever. The amplification in this case arises from the fact that once the differential acceleration has acted on the inflowing ISM bowshocks form around the denser components as they plough through the less dense regions. These bowshocks create a transverse velocity component which, due to flux freezing, then also creates a transverse magnetic field component. This transverse component can then be sheared in the same manner as the initial field in simulation adb-2d-std, thereby becoming amplified.

One might reasonably wish to know the mean amplification achieved if the magnetic field in the undisturbed medium is randomly oriented. We can calculate this mean amplification factor, $\langle \frac{B_f}{B_0} \rangle$, as

$$\left\langle \frac{B_f}{B_0} \right\rangle = \frac{2}{\pi} \int_0^{\frac{\pi}{2}} (\cos^2 \alpha + F^2 \sin^2 \alpha)^{\frac{1}{2}} d\alpha \approx 9.6 \quad (17)$$

presuming the angle between the magnetic field and the shock normal is a uniformly distributed random variable. This is likely to be approximately valid either for a supernova encountering an ISM with a highly turbulent magnetic field, or for the mean amplification measured over a large number of supernovae.

Thus, even allowing for variation in the orientation of the magnetic field, we can expect amplification of at least a factor of 10 over what would be expected from the pre-existing ISM magnetic field and standard shock physics.

4.3 Influence of radiative cooling

One of the implications of our model is that an ensemble of shocks which are significantly weaker than the blastwave of the supernova remnant itself will be formed as a result of the differential acceleration in the precursor. These shocks may be in the regime where significant radiative cooling can occur via line emission. This, at least in principle, raises the possibility that cooling itself may change the dynamics so as to enhance the magnetic field amplification. This might naively be expected since cooling typically leads to greater compression ratios (resulting from the radiating away of internal energy) and hence greater density contrasts, leading to greater differential acceleration and more rapid magnetic field amplification. Since this is a rather complex system it is not clear, however, whether radiative cooling will actually have any effect at all. We now turn our attention to studying the effect of including this in our simulations.

Figure 9 contains plots of the magnetic field amplification for adb-2d-std and cool-2d-std. It is interesting to see that, in fact, the addition of cooling via line emission has little impact on the overall amplification factor. A closer examination of Fig. 9 gives us some clue as to why this might be. In the range $3 \times 10^{17} \text{cm} \leq x \leq 4.5 \times 10^{17} \text{cm}$ there is slightly enhanced amplification. This enhancement disappears as we move towards $x = 5 \times 10^{17} \text{cm}$. This suggests that the cooling is most effective in this part of the flow. A further hint that this is the case is provided when we examine the vorticity. Figure 10

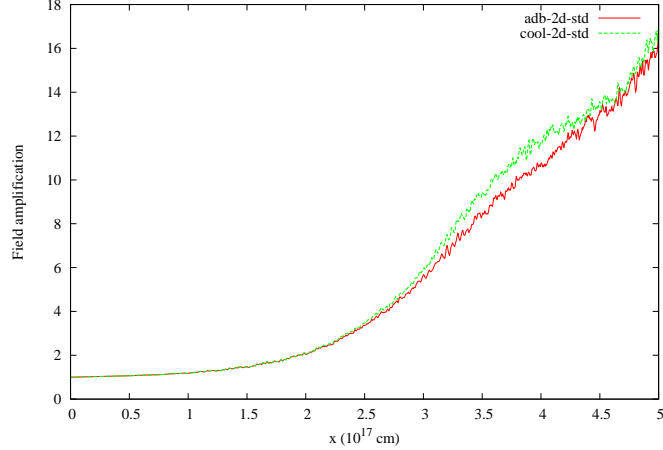


Figure 9: Plots of the magnetic field amplification for adb-2d-std and cool-2d-std. It can be concluded that the cooling makes rather little difference to the field amplification.

contains plots of the vorticity (normalised by the flow-time through the precursor without deceleration) for simulations adb-2d-std and cool-2d-std.

The vorticity in the flow contributes significantly to the magnetic field amplification. To see this, consider Figure 11 which contains a plot of the ratio of the magnetic field strength to the mass density as a function of x . If compression were the dominant mode of strengthening the field this ratio should remain constant for all x . In fact it increases to a value of 6, indicating that the magnetic field becomes 6 times stronger than would be expected from compression alone. As the ISM flows through the precursor the vorticity grows and, in turn, this amplifies the field leading to the maximum *growth* of the field occurring where there is high vorticity (cf Figs 9 and 10). It is clear from Fig. 10 that the vorticity does not grow monotonically as the flow proceeds through the precursor. In fact there is a peak located at approximately the centre of the computational domain, and the value of the vorticity at this peak is quite different in the cooled and adiabatic simulations. This difference in the vorticity is the cause of the enhanced field amplification in cool-2d-std. The vorticity decays as the flow moves further through the precursor. The vorticity causes efficient mixing of the high and low density parts of the ISM, reducing differential acceleration and leading to a reduction in the vorticity itself. For these parameters, where the initial magnetic field is weak in comparison to the energy available from differential acceleration, this is the saturation mechanism of the instability. Note that, physically, the lengthscales on which this mixing occurs is defined by the viscous or resistive lengthscales. In numerical simulations, on the other hand, it is defined by numerical viscosity which, for the *HYDRA* code becomes noticeable below lengthscales of around 10 – 15 zones (see Sect. 4.1). As noted in Paper I, mixing on unphysically large lengthscales will *reduce* the field amplification. Therefore we expect that the amplification achieved in our simulations is actually a *lower limit* for the amplification which would be achieved in the precursor of a supernova. We expect, however, that the saturation mechanism of the instability will remain qualitatively the same.

This mixing also reduces the influence of radiative cooling on the dynamics of the

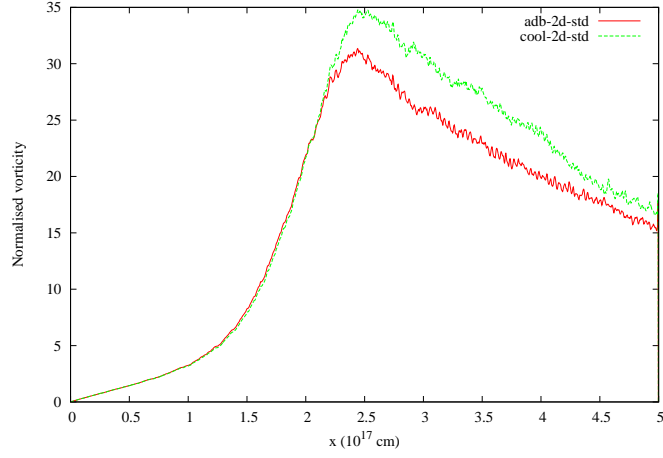


Figure 10: Plots of the vorticity normalised by the flow time through the precursor without deceleration (i.e. $\frac{t}{U_0}(\nabla \times \mathbf{u})$) for simulations adb-2d-std and cool-2d-std.

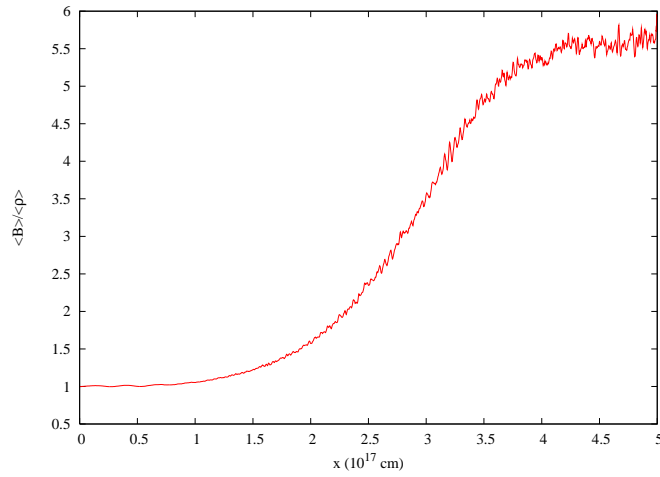


Figure 11: Plot of $\frac{B}{\rho}$, averaged in the y direction and normalised to its value at $x = 0$, for adb-2d-std. If compression were the dominant mechanism for amplifying the field then this ratio would be approximately 1 for all x .

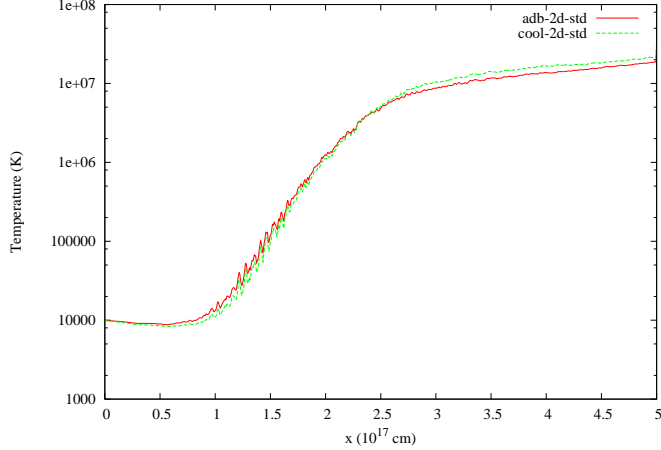


Figure 12: Plots of the mean temperature as a function of distance into the precursor for simulations adb-2d-std and cool-2d-std.

process: the high density regions are mixed with low density regions, and the shock strengths are reduced. This is not the only reason for the lack of influence of line emission on the dynamics however. Figure 12 shows plots of the mean temperature as a function of distance for adb-2d-std and cool-2d-std. Figure 13 contains a plot of the cooling function used in this work.

A comparison of these two figures demonstrates clearly that the region in which the fluid has a temperature at which cooling is significant (for example, the cooling coefficient is within an order of magnitude of the maximum) is between 1×10^{17} cm and 2×10^{17} cm. To get an idea of the likely influence of the cooling on the dynamics we calculate the cooling time, the ratio of the internal energy density of the gas to the rate of loss of energy density due to radiative cooling:

$$\tau_c = \frac{P}{(\gamma - 1)n^2\Lambda(T)} \quad (18)$$

Typical values in these simulations, with $n = 100 \text{ cm}^{-3}$ are between 10^8 s and 10^9 s. In this time the gas will be advected a distance of around $\geq 10^{17}$ cm - a lengthscale of order, or larger than, the time spent in the region on of the precursor in which the temperature leads to appreciable cooling.

To investigate this further, for higher cooling rates, we consider simulation adb-2d-hden. Figure 14 contains plots of the field amplification for adb-2d-std and cool-2d-hden, the latter being a simulation in which the incoming ISM density is arbitrarily raised to a value of 10^3 cm^{-3} . Since the cooling we are describing here is collisional, this increases the strength of the cooling by a factor of 100, and thus reduces the cooling length by the same factor. Comparing with Figure 9 we can see that, as expected, the cooling now leads to an enhanced amplification of the field. The final amplification factor (at $x = 5 \times 10^{17}$ cm) is approximately 23, instead of 16 for adb-2d-std. Investigation of the mean compression of the flow in these two simulations shows that each system results in mean compressions which are broadly similar, indicating that the enhanced amplification comes about as a result of the increased vorticity generated by the increased density contrasts in the

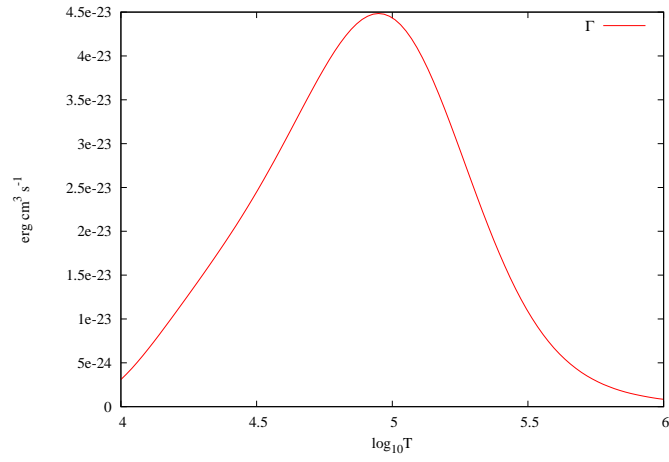


Figure 13: Plot of the cooling coefficient as a function of temperature used in this work.

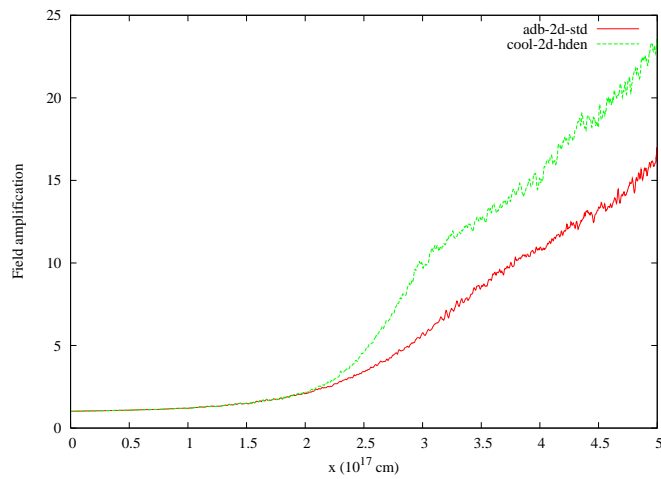


Figure 14: Plots of the field amplification as a function of distance for simulations adb-2d-std and cool-2d-hden.

radiatively cooled flow. This suggests that supernova blastwaves encountering density enhancements in the ISM, such as molecular clouds, will exhibit enhanced magnetic field amplification. Details of this mechanism are much more complicated in molecular cloud material, however, where cooling processes will include complex chemical networks and, possibly, multifluid effects. This is the subject of future work.

5 Conclusions

We have investigated in some detail the model originally presented in [Paper I](#), specifically with regard to the influence of the dimensionality of the turbulence, the angle of the magnetic field to the shock normal and the likely influence of collisional cooling. The following summarises our main conclusions:

1. 3D turbulence leads to field amplification which is slightly ($\sim 17\%$) less than that achieved for 2D turbulence. We attribute this to the inverse cascade in 2D leading to a concentration of turbulent kinetic energy at large scales,
2. the angle of the magnetic field plays a critical role in the level of field amplification achieved with values ranging between 5 and 17, depending on whether the shock normal is parallel or perpendicular to the prevailing magnetic field in the undisturbed ISM,
3. mean values of amplification that are achieved can be expected to be at least 10, when averaged over the possible angles between the magnetic field and the shock normal,
4. radiative cooling does not lead to appreciable impacts on the global dynamics of the system, primarily due to the speed with which the ISM propagates through the precursor region leading to the time it takes for the ISM to cool significantly being of order than, or longer than its residence time in the precursor. This result is modified if the blastwave encounters density enhancements, such as molecular clouds, in the ISM. In this case the field amplification is expected to be greater, though details of this mechanism in such an environment are complicated by energetically significant chemical reaction networks and, possibly, multifluid effects.

The model presented in [Paper I](#) appears to be robust to considerations such as the magnetic field orientation, the presence of collisional cooling and the dimensionality of the simulations. Note that, in keeping with the philosophy of [Paper I](#), we have neglected the details of the behaviour of the diffusion coefficient (e.g. its dependence on the field orientation). Nonetheless, it seems that our overall conclusion, namely that this model can produce the field amplification required to explain the observations, is generally applicable to SNRs in a variety of environments and with a variety of parameters.

Acknowledgements

The authors wish to acknowledge the SFI/HEA Irish Centre for High-End Computing (ICHEC) for the provision of computational facilities and support. TPD would like to

thank Aoife Curran for discussions of the power spectra of the simulations. We would also like to acknowledge the helpful comments of the anonymous referee.

References

- Ballet J., 2006, *Advances in Space Research*, 37, 1902 (Cited on page 2.)
- Bamba A., Ueno M., Nakajima H., Koyama K., 2004, *ApJ*, 602, 257 (Cited on page 2.)
- Bamba A., Yamazaki R., Yoshida T., Terasawa T., Koyama K., 2005, *ApJ*, 621, 793 (Cited on page 2.)
- Begelman M. C., Zweibel E. G., 1994, *ApJ*, 431, 689 (Cited on page 2.)
- Bell A. R., 2004, *MNRAS*, 353, 550 (Cited on page 2.)
- Beresnyak A., Jones T. W., Lazarian A., 2009, *ApJ*, 707, 1541 (Cited on page 2.)
- Berezhko E. G., Ksenofontov L. T., Völk H. J., 2003, *A&A*, 412, L11 (Cited on page 2.)
- Brio M., Wu C. C., 1988, *Journal of Computational Physics*, 75, 400 (Cited on page 21.)
- Brüggen M., 2013, *MNRAS*, 436, 294 (Cited on pages 3 and 10.)
- Dahlburg R. B., Picone J. M., 1989, *Physics of Fluids B*, 1, 2153 (Cited on page 22.)
- Dai W., Woodward P. R., 1998, *ApJ*, 494, 317 (Cited on page 23.)
- Dedner A., Kemm F., Kröner D., Munz C.-D., Schnitzer T., Wesenberg M., 2002, *Journal of Computational Physics*, 175, 645 (Cited on page 5.)
- Downes T. P., 2012, *MNRAS*, 425, 2277 (Cited on page 10.)
- Drury L. O., Downes T. P., 2012, *MNRAS*, 427, 2308 (Cited on pages 2, 3, 4, 6, 13, 15, and 19.)
- Drury L. O., Falle S. A. E. G., 1986, *MNRAS*, 223, 353 (Cited on page 2.)
- Falle S. A. E. G., Komissarov S. S., Joarder P., 1998, *MNRAS*, 297, 265 (Cited on page 22.)
- Gaetz T. J., Edgar R. J., Chevalier R. A., 1988, *ApJ*, 329, 927 (Cited on page 5.)
- Lagage P. O., Cesarsky C. J., 1983, *A&A*, 125, 249 (Cited on page 2.)
- Londrillo P., Del Zanna L., 2000, *ApJ*, 530, 508 (Cited on page 23.)
- Orszag S. A., Tang C.-M., 1979, *Journal of Fluid Mechanics*, 90, 129 (Cited on page 22.)
- O’Sullivan S., Downes T. P., 2006, *MNRAS*, 366, 1329 (Cited on pages 4 and 5.)
- O’Sullivan S., Downes T. P., 2007, *MNRAS*, 376, 1648 (Cited on pages 4 and 5.)

- Parizot E., Marcowith A., Ballet J., Gallant Y. A., 2006, *A&A*, 453, 387 (Cited on page 2.)
- Picone J. M., Dahlburg R. B., 1991, *Physics of Fluids B*, 3, 29 (Cited on page 22.)
- Ryu D., Kang H., Jones T. W., 1993, *ApJ*, 405, 199 (Cited on page 2.)
- Sutherland R. S., Dopita M. A., 1993, *ApJS*, 88, 253 (Cited on page 5.)
- Uchiyama Y., Aharonian F. A., Tanaka T., Takahashi T., Maeda Y., 2007, *Nature*, 449, 576 (Cited on page 2.)
- Vink J., 2012, *A&A Rev.*, 20, 49 (Cited on pages 2 and 5.)
- Vink J., Laming J. M., 2003, *ApJ*, 584, 758 (Cited on page 2.)
- Völk H. J., Berezhko E. G., Ksenofontov L. T., 2005, *A&A*, 433, 229 (Cited on page 2.)
- Webb G. M., Zakharian A., Zank G. P., 1999, *Journal of Plasma Physics*, 61, 553 (Cited on page 2.)
- Yamazaki R., Yoshida T., Terasawa T., Bamba A., Koyama K., 2004, *A&A*, 416, 595 (Cited on page 2.)

Appendix A Sample Ideal MHD tests for *HYDRA*

The *HYDRA* code has been extensively tested for both ideal and multifluid MHD, as noted in Sect. 3. The code is maintained using the `subversion`¹ versioning system and each night the latest version of the code is automatically downloaded from the main repository and tested against a number of tests. Each week a full suite of tests is run on the latest version of the code. In this section we provide two of the ideal MHD tests we use to demonstrate the effectiveness of *HYDRA* in simulating ideal MHD systems. The Brio-Wu shocktube test demonstrates the shock-capturing nature of the code, while the Orszag-Tang vortex is useful to test the multidimensional performance of the code. Both of these are standard tests used in the literature.

A.1 Brio-Wu Shocktube test

This is a 1D test proposed by Brio & Wu (1988) in which a left and right state are defined and are initially separated by a discontinuity. Once the system begins to evolve this discontinuity breaks down into a series of shocks and rarefactions of waves of different types. Using the notation that \mathbf{u} is the state vector, with $\mathbf{u} = (\rho, u_x, u_y, u_z, P, B_x, B_y, B_z)^T$, the

¹See <http://subversion.apache.org/>.

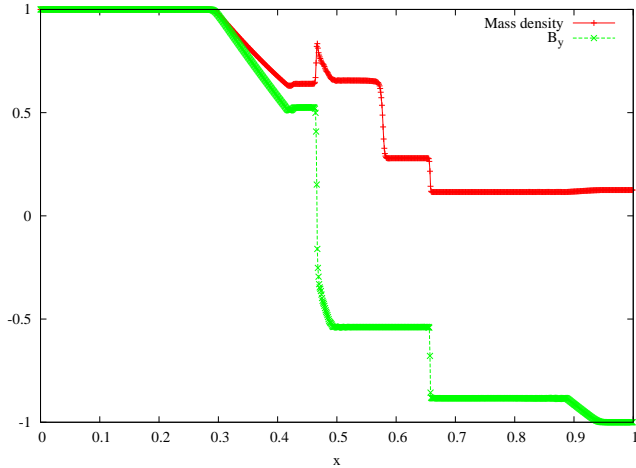


Figure 15: Plots of the mass density and the y component of the magnetic field at $t = 0.12$ for the Brio-Wu shocktube test.

initial conditions are as follows:

$$\mathbf{u}_L = \begin{pmatrix} 1 \\ 0 \\ 0 \\ 0 \\ 1 \\ 0.75 \\ 1 \\ 0 \end{pmatrix} \quad \mathbf{u}_R = \begin{pmatrix} 0.125 \\ 0 \\ 0 \\ 0 \\ 0.1 \\ 0.75 \\ -1 \\ 0 \end{pmatrix}. \quad (19)$$

The initial discontinuity is positioned at $x = 0.5$ and we use 1000 grid points in the test presented here.

Figure 15 contains plots of the density, ρ , and the y component of the magnetic field as a function of x at time 0.12. These results can be compared with those presented in, for example, [Falle et al. \(1998\)](#). It can be seen that the results match those in the literature rather well.

A.2 The Orszag-Tang Vortex test

This test was first studied by [Orszag & Tang \(1979\)](#) for the incompressible case, and subsequently by [Dahlburg & Picone \(1989\)](#) and [Picone & Dahlburg \(1991\)](#) for the compressible case presented here. It is widely used as a test of the performance of multidimensional MHD codes in tracking the evolution of shocks and the transition to turbulence of an

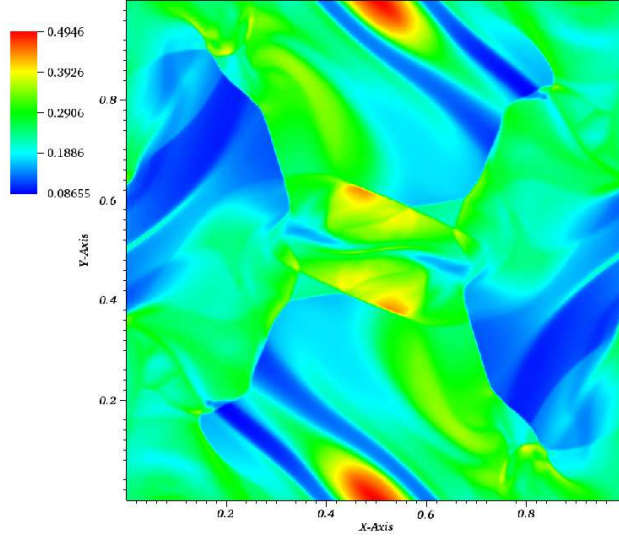


Figure 16: Distribution of mass density in the Orszag-Tang vortex test at $t = 0.5$.

initially non-turbulent medium. The initial conditions used are

$$\mathbf{u} = \begin{pmatrix} \frac{25}{36\pi} \\ \sin(2\pi y) \\ \sin(2\pi x) \\ 0 \\ \frac{5}{12\pi} \\ -\frac{1}{(4\pi)^{1/2}} \sin(2\pi y) \\ \frac{1}{(4\pi)^{1/2}} \sin(4\pi x) \\ 0 \end{pmatrix} \quad (20)$$

using the notation defined in A.1 for the definition of the state vector. The simulation is run on a unit square using 512×512 grid zones and periodic boundary conditions in all directions.

Figure 16 contains a plot of the distribution of the mass density at $t = 0.5$. This can be seen to compare well with Figure 6 of Dai & Woodward (1998) and Figure 10 of Londrillo & Del Zanna (2000). Figure 17 contains a plot of the pressure at $y = 0.3125$ at $t = 0.5$. This plot can be compared with the lower panel in Figure 11 of Londrillo & Del Zanna (2000). In all cases the results of *HYDRA* for ideal MHD can be seen to match well with those published by other authors using a variety of codes and algorithms, indicating that we can have some confidence in the results presented here.

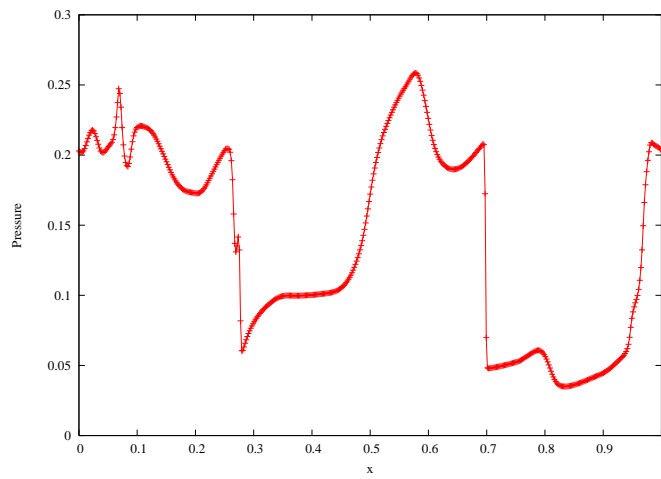


Figure 17: Plot of the thermal pressure in the Orszag-Tang vortex test at $t = 0.5$ and $y = 0.3125$. temperature used in this work.